

Synthetic aperture radar imaging exploiting multiple scattering

This article has been downloaded from IOPscience. Please scroll down to see the full text article.

2011 Inverse Problems 27 055004

(<http://iopscience.iop.org/0266-5611/27/5/055004>)

View [the table of contents for this issue](#), or go to the [journal homepage](#) for more

Download details:

IP Address: 64.134.71.68

The article was downloaded on 31/03/2011 at 00:37

Please note that [terms and conditions apply](#).

Synthetic aperture radar imaging exploiting multiple scattering

V Krishnan¹ and B Yazici²

¹ Department of Mathematics, University of Bridgeport, Bridgeport, CT 06604, USA

² Department of Electrical, Computer and Systems Engineering, Rensselaer Polytechnic Institute, Troy, NY 12180-3590, USA

E-mail: venkatek@bridgeport.edu and yazici@ecse.rpi.edu

Received 21 August 2010, in final form 18 January 2011

Published 29 March 2011

Online at stacks.iop.org/IP/27/055004

Abstract

In this paper, we consider an imaging scenario, where a bi-static synthetic aperture radar (SAR) system is used in a multiple scattering environment. We consider a ray-theoretic approximation to the Green function to model a multiple scattering environment. This allows us to incorporate the multiple paths followed by the transmitted signal, thereby providing different views of the object to be imaged. However, the received signal from the multiple paths and additive thermal noise may interfere and produce artifacts when standard backprojection-based reconstruction algorithms are used. We use microlocal analysis in a statistical setting to develop a novel filtered-backprojection type image reconstruction method that not only exploits the multi-paths leading to enhancement of the reconstructed image but also suppresses the artifacts due to interference. We assume *a priori* knowledge of the second-order statistics of the target and noise to suppress the artifacts due to interference in a mean-square error sense. We present numerical simulations to demonstrate the performance of our image reconstruction method. While the focus of this paper is on radar applications, our image formation method is also applicable to other problems arising in fields such as acoustic, geophysical and medical imaging.

(Some figures in this article are in colour only in the electronic version)

1. Introduction

In synthetic aperture radar (SAR) imaging, a scene of interest is illuminated by electromagnetic (EM) waves transmitted from an antenna deployed on a moving platform such as an airplane or satellite. An image of the scene is reconstructed from the measurement of the back-scattered EM waves at the receiver antenna.

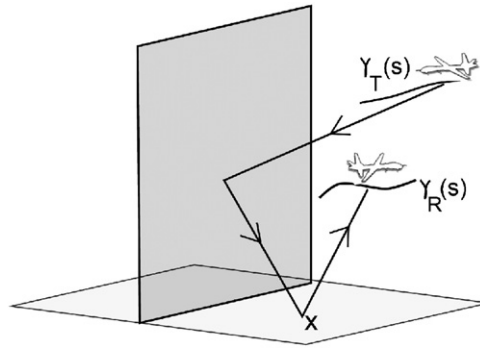


Figure 1. A bi-static SAR system exploiting a multi-path afforded by the presence of a vertical wall in the vicinity of a target.

In mono-static SAR, the transmitter and receiver antennas are co-located. The bi-static SAR system involves transmitter and receiver antennas that are several wavelengths apart. Conventional SAR image formation methods rely on the single-scattering assumption in free-space. However, this assumption does not necessarily hold in many situations, where scattering can follow multiple paths (multi-paths) between the SAR platforms and the scene.

In recent years there have been studies toward understanding and incorporating multi-path scattering in SAR image reconstruction. In [6–10, 18], the authors developed image reconstruction algorithms for multi-path scattering in SAR and tomographic medical imaging. Tracking of moving targets in a multi-path urban environment has been studied in [19] and [14]. References [2] and [17] have shown that proper incorporation of multi-path information offers potential gains in imaging such as wider aperture and higher resolution. In [2], a medium with point-like scatterers was considered and an imaging method that exploits multi-path between the scene of interest and these point-like scatterers was developed. It was shown that multi-path scattering incorporates views from extra directions and enhances image resolution. In [5, 17], a vertical perfectly reflecting wall adjacent to the scene of interest was considered. Under the assumption that the receiver platform can isolate the EM waves scattered from different scattering paths, it was shown in [17] that taking into account multi-path scattering enhances the image resolution. In a follow-up work [5], dropping the assumption that a receiver can decompose the data from different scattering paths, the structure of the artifacts introduced by backprojection algorithms was studied.

In this paper, we consider a simple multi-path imaging environment where the object of interest is in the vicinity of a known perfectly reflecting vertical wall and a bi-static SAR system is used in imaging the object; see figure 1. We assume that the transmitter and receiver are traversing arbitrary, but known, trajectories. We incorporate the multi-paths that the transmitted signal can take in the presence of this wall into our received data. Furthermore, we assume that the receiver *cannot* isolate the data due to the different scattering paths. Due to this assumption, the data from different scattering paths interfere to produce artifacts in the final image when the measurements are backprojected.

We derive a filtered-backprojection (FBP) algorithm that exploits multi-path scattering. Our work differs from the earlier works in the following way: we show that exploiting multi-path not only enhances image resolution, but also that the artifacts that appear due to application of previously known backprojection-type algorithms can be suppressed. While the structure of these artifacts is studied in [5], to the best of our knowledge, our work is the first to address how these artifacts can be suppressed.

Similar to the work [13, 23], we use microlocal analysis in a statistical setting to develop our image reconstruction method. Microlocal techniques lead to inversion methods that have the desirable property that visible edges in the scene will appear in the reconstructed image at the correct location and orientation [11, 20, 21]. They can also account for various factors such as an arbitrary flight trajectory, non-flat ground topography, antenna beam pattern, transmitted waveform and geometric spreading. Furthermore, microlocal techniques give rise to FBP-type inversion, which is a direct (noniterative) method and can be implemented fast [16].

Given the different scattering paths, we treat the multi-path imaging set-up similar to a multi-static setting involving the trajectories of a transmitter and receiver and their virtual counterparts obtained by reflections about the vertical wall. We employ the techniques introduced in [13, 23] to reconstruct the image of the target while suppressing the artifacts caused by data interference from different scattering paths. As in [13], our method involves backprojecting the received data with respect to each transmitter-receiver pair. We assume that we have *a priori* knowledge of the second-order statistics of the target to be reconstructed. We determine the second-order statistics of the artifacts caused by interference based on different scattering paths and design a filter that preserves the singularities in the received data due to the scene while suppressing the strength of the artifact singularities in the mean-square error (MSE) sense. We form the final image by superposition of images reconstructed for all different multi-paths.

This paper is organized as follows. In section 2, we introduce the multi-path SAR forward model in a deterministic and statistical setting. In section 3, we introduce the FBP-type image reconstruction operators and derive the filters. Numerical simulations are presented in section 5, and section 6 concludes the paper. The stationary phase method on which our filter derivations are based is given in appendix A. The derivations involved in the construction of the filters are given in appendices B, C, D and E.

2. Forward model for multi-path SAR

2.1. Notation

We use the following notational conventions in this paper. Operators are denoted in calligraphic font, points in \mathbb{R}^n for $n \geq 3$, \mathbb{R}^2 and \mathbb{R} are denoted in bold Roman, bold italic and italic letters, respectively. Table 1 includes all other notations used in the paper.

2.2. Deterministic forward model

We consider an imaging scenario where the target of interest is in the vicinity of a perfectly reflecting vertical wall. For the analysis that follows, we make the simplifying assumption that the wall is infinite. However, in reality, a wall is finite and therefore only a part of the target due to reflections from the finite wall can be reconstructed. The finiteness of the wall can be taken into account by setting the antenna beam patterns (the amplitude term A_j in (15)) to be 0 when reflection occurs at points not belonging to the known finite wall. Also the assumption that the wall is perfectly reflecting simplifies our analysis. With minor modifications, our method will work when the reflection parameters of the wall are known.

We assume that a bi-static SAR system is employed in imaging the scene with the transmitter and receiver trajectories denoted by $\gamma_T(s) \in \mathbb{R}^3$ and $\gamma_R(s) \in \mathbb{R}^3$ for $s \in \mathbb{R}$, respectively. We are interested in obtaining a linearized model for the scattered signal at the receiver in the presence of this vertical wall in the background medium.

Table 1. Notation

Symbol	Designation
T	Scene reflectivity function
s	Slow-time
t	Fast-time
c_0	Speed of light in free space
$\mathbf{x} = (x, \psi(x))$	Earth's surface
$\hat{\mathbf{z}}$	Unit vector in the direction of $\mathbf{z} \in \mathbb{R}^3$
ω	Temporal frequency variable
γ_T	Trajectory of the transmitter
$\tilde{\gamma}_T$	Mirror trajectory of γ_T with respect to a vertical plane
γ_R	Trajectory of the receiver
$\tilde{\gamma}_R$	Mirror trajectory of γ_R with respect to a vertical plane
$R_{TR}(s, x)$	Bistatic distance traveled by the signal from the antenna location $\gamma_T(s)$ to the ground location \mathbf{x} and then to the receiver location $\gamma_R(s)$
Ω_z^j	Data collection manifold for the j th multi-path for a pixel at \mathbf{z}
d	Total received signal at the receiver from different multi-paths
n	Additive noise at the receiver
R_T	Autocorrelation function of T
S_T	Power spectral density function of T
R_n	Autocorrelation function of n
S_n	Power spectral density function of additive noise at the q th receiver
E	Expectation operator
\mathcal{F}_j	Multi-path forward model for the ideal data at the receiver due to the j th multi-path
\mathcal{K}_j	filtered-backprojection operator with respect to the j th multi-path
B_j	reconstruction filter for the j th multi-path

We first consider wave propagation in the region near the vertical wall. The propagation of EM waves can be described by the scalar wave equation:

$$\left(\nabla^2 - \frac{1}{c^2} \partial_t^2\right) E(\mathbf{x}, t) = P(t) \delta(\mathbf{x} - \gamma_T(s)), \quad (1)$$

where c is the speed of EM waves in the medium, $E(\mathbf{x}, t)$ is the electric field, $\gamma_T(s)$ denotes a one-parameter curve for the trajectory of the transmitter, s and t are called the slow- and fast-time variables, respectively, and $P(t)$ is the transmitted waveform. The wave speed c is spatially varying due to inhomogeneities present in the medium. We assume that the background in which the EM waves propagate is free space. Therefore c can be expressed as

$$\frac{1}{c^2(\mathbf{x})} = \frac{1}{c_0^2} + \tilde{T}(\mathbf{x}), \quad (2)$$

where the constant c_0 is the speed of light in free space and $\tilde{T}(\mathbf{x})$ is the perturbation due to the deviation from the background, referred to as the target reflectivity function, which we wish to recover from backscattered waves.

Since the incident EM waves in typical radar frequencies attenuate rapidly as they penetrate the ground, we assume that $\tilde{T}(\mathbf{x})$ varies only on a two-dimensional surface. Therefore, we represent \tilde{T} as a function of the form

$$\tilde{T}(\mathbf{x}) = T(x) \delta_0(x_3 - \psi(x)) \quad (3)$$

where $\mathbf{x} = (x, x_3)$ and $\psi : \mathbb{R}^2 \rightarrow \mathbb{R}$ is a smooth function of $\mathbf{x} = (x_1, x_2) \in \mathbb{R}^2$ representing the ground topography.

Now without loss of generality, let us assume that the vertical wall is along $x_1 = 0$, the target on the ground is in the region $x_1 > 0$, and the trajectories of the transmitter and receiver are on the same side of the wall as the target. Also for simplicity we assume that the solution E to the wave equation (1) at points on the wall satisfies the condition:

$$E(\mathbf{x}, t)|_{x_1=0} = 0. \tag{4}$$

The background Green function g is then given by the solution to the following equation:

$$\left(\nabla^2 - \frac{1}{c_0^2} \partial_t^2\right) g(\mathbf{x}, \gamma_T(s), t) = \delta(\mathbf{x} - \gamma_T(s))\delta(t), \quad \text{for } x_1 > 0$$

$$g|_{x_1=0} = 0.$$

Using the method of images, we can explicitly write g as

$$g(\mathbf{x}, \gamma_T(s), t) = \frac{\delta(t - |\mathbf{x} - \gamma_T(s)|/c_0)}{4\pi|\mathbf{x} - \gamma_T(s)|} - \frac{\delta(t - |\mathbf{x} - \tilde{\gamma}_T(s)|/c_0)}{4\pi|\mathbf{x} - \tilde{\gamma}_T(s)|}, \tag{5}$$

where $\tilde{\gamma}_T(s)$ is the *virtual* point source location obtained by reflection of the location of the real point source about the vertical wall. Using (5), the incident field E^{in} due to the source $s(\mathbf{x}, t) = P(t)\delta(\mathbf{x} - \gamma_T(s))$ is given as

$$E^{\text{in}}(\mathbf{x}, t) = \int g(\mathbf{x}, \mathbf{y}, t - \tau) s(\mathbf{y}, \tau) d\mathbf{y} d\tau \tag{6}$$

$$= \frac{P(t - |\mathbf{x} - \gamma_T(s)|/c_0)}{4\pi|\mathbf{x} - \gamma_T(s)|} - \frac{P(t - |\mathbf{x} - \tilde{\gamma}_T(s)|/c_0)}{4\pi|\mathbf{x} - \tilde{\gamma}_T(s)|}. \tag{7}$$

Let E denote the total field of the medium, $E = E^{\text{in}} + E^{\text{sc}}$. Then, the scattered field is given by the following Lippman–Schwinger equation:

$$E^{\text{sc}}(\mathbf{z}, t) = \int g(\mathbf{z}, \mathbf{x}, t - \tau) \partial_t^2 E(\mathbf{x}, \tau) T(\mathbf{x}) d\mathbf{x} d\tau, \tag{8}$$

where $\mathbf{x} = (x, \psi(x))$. We linearize (8) by the first Born approximation and write the scattered wave-field at the receiver location $\gamma_R(s)$ as follows:

$$E^{\text{sc}}(\gamma_R(s), t) \approx \int g(\gamma_R(s), \mathbf{x}, t - \tau) \partial_t^2 E^{\text{in}}(\mathbf{x}, \tau) T(\mathbf{x}) d\mathbf{x} d\tau$$

$$= \iint \left(\frac{\delta(t - \tau - |\mathbf{x} - \gamma_R(s)|/c_0)}{4\pi|\mathbf{x} - \gamma_R(s)|} - \frac{\delta(t - \tau - |\mathbf{x} - \tilde{\gamma}_R(s)|/c_0)}{4\pi|\mathbf{x} - \tilde{\gamma}_R(s)|} \right)$$

$$\times \left(e^{-i\omega(\tau - |\mathbf{x} - \gamma_T(s)|/c_0)} \frac{\omega^2 p(\omega)}{4\pi|\mathbf{x} - \gamma_T(s)|} - e^{-i\omega(\tau - |\mathbf{x} - \tilde{\gamma}_T(s)|/c_0)} \frac{\omega^2 p(\omega)}{4\pi|\mathbf{x} - \tilde{\gamma}_T(s)|} \right)$$

$$\times T(\mathbf{x}) d\omega d\mathbf{x} d\tau, \tag{9}$$

where p is the Fourier transform of P .

Now, integrating (9) with respect to τ , a model for the scattered signal $d(s, t)$ at *slow-time* s and *fast-time* t is given as follows:

$$d(s, t) := E^{\text{sc}}(\gamma_R(s), t) = \int e^{-i\omega(t - R_{TR}(s, \mathbf{x})/c_0)} A_{TR}(s, \mathbf{x}, \omega) T(\mathbf{x}) d\mathbf{x} d\omega \tag{10}$$

$$+ \int e^{-i\omega(t - R_{\tilde{T}R}(s, \mathbf{x})/c_0)} A_{\tilde{T}R}(s, \mathbf{x}, \omega) T(\mathbf{x}) d\mathbf{x} d\omega \tag{11}$$

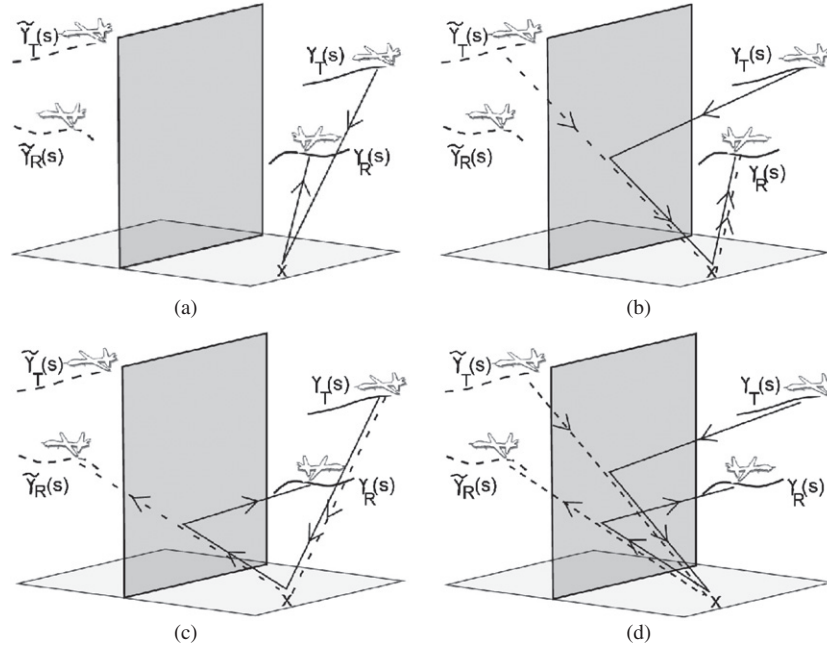


Figure 2. The four scattering paths in multi-path SAR set-up involving a vertical wall. $\gamma_T(s)$ and $\gamma_R(s)$ denote the transmitter and receiver trajectories, and $\tilde{\gamma}_T(s)$ and $\tilde{\gamma}_R(s)$ denote the virtual transmitter and virtual receiver trajectories.

$$+ \int e^{-i\omega(t-R_{T\tilde{R}}(s,\mathbf{x})/c_0)} A_{T\tilde{R}}(s, \mathbf{x}, \omega) T(\mathbf{x}) d\mathbf{x} d\omega \tag{12}$$

$$+ \int e^{-i\omega(t-R_{\tilde{T}R}(s,\mathbf{x})/c_0)} A_{\tilde{T}R}(s, \mathbf{x}, \omega) T(\mathbf{x}) d\mathbf{x} d\omega \tag{13}$$

where $R_{TR}(s, \mathbf{x}) = |\gamma_T(s) - \mathbf{x}| + |\mathbf{x} - \gamma_R(s)|$ is the bi-static distance and $A_{TR}(s, \mathbf{x}, \omega) = p(\omega)((4\pi)^2|\gamma_T(s) - \mathbf{x}||\gamma_R(s) - \mathbf{x}|)^{-1}$. The expressions involving ‘tilde’ in equations (11)–(13) involve virtual transmitter and receiver trajectories obtained by reflections of the transmitter and receiver trajectories about the vertical wall. For example, $R_{T\tilde{R}}(s, \mathbf{x}) = |\gamma_T(s) - \mathbf{x}| + |\mathbf{x} - \tilde{\gamma}_R(s)|$ and $A_{T\tilde{R}}(s, \mathbf{x}, \omega)$ is approximated by $A_{\tilde{T}R}(s, \mathbf{x}, \omega) = -p(\omega)((4\pi)^2|\gamma_T(s) - \mathbf{x}||\tilde{\gamma}_R(s) - \mathbf{x}|)^{-1}$. Note that the four terms in equations (10)–(13) model the scattered signal from the four paths, respectively, as shown in figure 2.

For notational convenience, from now on, unless otherwise stated, we replace the subscripts $TR, \tilde{T}R, T\tilde{R}$ and $\tilde{T}\tilde{R}$ in (10)–(13) with 1, 2, 3 and 4, respectively.

We now write $d(s, t)$ as

$$d(s, t) = (\mathcal{F}_1 + \mathcal{F}_2 + \mathcal{F}_3 + \mathcal{F}_4) [T](s, t), \tag{14}$$

where

$$\mathcal{F}_j(s, t) = \int e^{-i\omega(t-R_j(s,\mathbf{x})/c_0)} A_j(s, \mathbf{x}, \omega) T(\mathbf{x}) d\mathbf{x} d\omega \tag{15}$$

for $j = 1, \dots, 4$.

We assume that the functions $A_j(s, \mathbf{x}, \omega)$ satisfy the following estimate for some real number m_j :

$$|\partial_\omega^\alpha \partial_s^\beta \partial_{x_1}^{\rho_1} \partial_{x_2}^{\rho_2} A_j(s, \mathbf{x}, \omega)| \leq C(1 + |\omega|^2)^{(m_j - |\alpha|)/2} \quad \text{for } (s, \mathbf{x}) \in K \text{ and } \omega \in \mathbb{R} \tag{16}$$

where $K \subset \mathbb{R} \times \mathbb{R}^2$ is any compact set and α and β , ρ_1 , ρ_2 are any non-negative integers, and C is a constant in terms of j , K , α , β , ρ_1 , ρ_2 . These estimates are satisfied when the antenna is broadband and when the source waveform is a band limited waveform. These assumptions are needed to make various stationary phase calculations. Furthermore, these assumptions make each operator \mathcal{F}_j a *Fourier integral operator* [4, 20, 21].

2.3. Statistical forward model

In this section, we model the target reflectivity as a random field and take into account the additive thermal noise at the receiver to model the measurements in a multi-path environment. We use this statistical forward model in developing an image formation method.

In the presence of thermal noise and random target reflectivity function, we consider the following model for the measurement at the receiver:

$$d(s, t) = \sum_{j \in \text{paths}} \mathcal{F}_j[T](s, t) + n(s, t) \quad (17)$$

where n denotes the thermal noise at the receiver and \mathcal{F}_j is defined as in (15).

Without loss of generality, we assume that T and n are zero-mean random processes. That is,

$$E[T(\mathbf{x})] = 0 \quad \text{for } \mathbf{x} \in \mathbb{R}^2 \quad (18)$$

$$E[n(s, t)] = 0 \quad \text{for } (s, t) \in [s_0, s_1] \times [t_0, t_1] \quad (19)$$

where E denotes the expectation operator.

We assume that T is stationary, and n is statistically uncorrelated in slow-time variable s and stationary in fast-time variable t . Let

$$R_T(\mathbf{x}; \mathbf{x}') = E[T(\mathbf{x})\overline{T(\mathbf{x}')}] \quad \text{for } \mathbf{x}, \mathbf{x}' \in \mathbb{R}^2 \quad (20)$$

$$R_n(s, t; s', t') = E[n(s, t)\overline{n(s', t')}] \quad \text{for } (s, t), (s', t') \in [s_0, s_1] \times [t_0, t_1]. \quad (21)$$

We next define

$$\tilde{S}_T(\zeta, \zeta') = \frac{1}{(2\pi)^4} \int e^{i(\mathbf{x} \cdot \zeta - \mathbf{x}' \cdot \zeta')} R_T(\mathbf{x}; \mathbf{x}') d\mathbf{x} d\mathbf{x}'. \quad (22)$$

With the stationarity assumption,

$$\tilde{S}_T(\zeta, \zeta') = S_T(\zeta)\delta(\zeta - \zeta'), \quad (23)$$

where S_T is the power spectral density function of T .

Similarly, we define

$$\tilde{S}_n(s, \omega, s', \omega') = \frac{1}{(2\pi)^2} \int e^{i(\omega t - \omega' t')} R_n(s, t; s', t') dt dt'. \quad (24)$$

Under the assumptions that n is stationary in t and statistically uncorrelated in s , \tilde{S}_n satisfies

$$\tilde{S}_n(s, \omega; s', \omega') = S_n(s, \omega)\delta(s - s')\delta(\omega - \omega') \quad (25)$$

where $S_n(s, \omega)$ is the power spectral density function of n at each slow-time s .

Finally, we assume that the random processes T and n are statistically uncorrelated. Thus,

$$E[T(\mathbf{x})n(s, t)] = 0 \quad \text{for all } \mathbf{x} \in \mathbb{R}^2, (s, t) \in [s_0, s_1] \times [t_0, t_1]. \quad (26)$$

In summary, the multi-path model we use in this paper is given by

$$d(s, t) = \sum_{j=1}^4 \mathcal{F}_j[T](s, t) + n(s, t), \quad (27)$$

where \mathcal{F}_j is defined in (15), T and n are random processes satisfying the properties stated above. Note that all the integrals appearing in \mathcal{F}_j for each path j are defined in the mean-square sense.

3. Image formation via filtered-backprojection

We now develop an FBP-type image reconstruction method for the multi-path SAR problem. We employ the techniques we developed in [13] in our reconstruction method. We fix a multi-path j and define an FBP reconstruction operator with respect to this multi-path. This backprojection operator reconstructs the visible edges of the target scene at the correct location and orientation, but the measurements from different multi-paths and receiver noise interfere with the data measured from path j , and these introduce artifacts in the reconstructed image. We derive a filter for the path j that not only reconstructs the visible edges of the scene at the correct location and orientation, but also suppresses the strength of the artifacts due to other multi-paths and receiver noise.

We design the filter for the j th path in the minimum MSE sense such that the frequency components of the target in the data collection manifold (defined below) for the j th path is preserved, whereas the frequency components of the artifacts are suppressed.

From now on, we fix the j th path to be the following:

$$\text{Transmitter} \rightarrow \text{Target} \rightarrow \text{Wall} \rightarrow \text{Receiver}. \quad (28)$$

The j th path corresponds to the following equivalent bi-static path:

$$\text{Transmitter} \rightarrow \text{Target} \rightarrow \text{Virtual Receiver}. \quad (29)$$

The j th path given in (28) and the equivalent bi-static path given in (29) are indicated by the solid and dotted lines, respectively, in figure 2(c).

The data collection manifold for this path is given as follows [22]:

$$\Omega_{\mathbf{z}}^j := \left\{ \frac{\omega}{c_0} D(z_1, z_2)^T (\mathbf{z} - \widehat{\gamma}_T(s) + \mathbf{z} - \widehat{\gamma}_R(s)) : A_j(\mathbf{z}, s, \omega) \neq 0 \right\} \quad (30)$$

with

$$D(z_1, z_2) = \begin{pmatrix} 1 & 0 \\ 0 & 1 \\ \frac{\partial \psi}{\partial z_1} & \frac{\partial \psi}{\partial z_2} \end{pmatrix}. \quad (31)$$

The superscript T denotes the transpose of the matrix $D(z_1, z_2)$ and $\widehat{\mathbf{x}}$ denotes the unit vector in the direction of \mathbf{x} .

3.1. Backprojection operators

We define the filtered backprojection operator for the multi-path data d with respect to the j th multi-path of (28) as

$$\mathcal{K}_j[d](\mathbf{z}) = \int e^{i\omega(t - \frac{1}{c_0}|\mathbf{z} - \widehat{\gamma}_T(s)| + |\mathbf{z} - \widehat{\gamma}_R(s)|)} B_j(\mathbf{z}, s, \omega) d(s, t) ds dt d\omega \quad (32)$$

where B_j is the filter to be determined. Let \widehat{T}_j be the image reconstructed by \mathcal{K}_j . That is,

$$\widehat{T}_j(\mathbf{z}) := \mathcal{K}_j[d](\mathbf{z}). \quad (33)$$

To study the point spread function of the imaging operator \mathcal{K}_j , we substitute (27) into (33) and obtain

$$\widehat{T}_j(\mathbf{z}) = \mathcal{K}_j \mathcal{F}_j[T](\mathbf{z}) + \sum_{k=1, k \neq j}^4 \mathcal{K}_j \mathcal{F}_k[T](\mathbf{z}) + \mathcal{K}_j n(\mathbf{z}). \quad (34)$$

Note that $\mathcal{K}_j \mathcal{F}_j$ is the bi-static SAR image reconstruction operator presented in [22]. This is a pseudodifferential operator and hence applying this operator to the scene reflectivity

function T preserves the edges of T at the correct location and orientation in the reconstructed image. All the other operators $\mathcal{K}_j \mathcal{F}_k$ for $k \neq j$ are not necessarily pseudodifferential operators, so they do not reconstruct the edges of T at the correct location. We design the filter B_j such that the singularities of the target in the data collection manifold corresponding to the j th multi-path is preserved while the additional singularities due to artifacts corresponding to all the other multi-paths and the receiver noise are suppressed in the minimum MSE sense.

3.2. Enhanced resolution exploiting multi-path scattering

In this subsection, we show that exploiting multi-path scattering can lead to increased resolution for the reconstructed image.

We consider the deterministic forward model $d(s, t)$ defined in subsection 2.2 and show that each summand in $d(s, t)$ defined by (10)–(13) approximately measures the Fourier transform of the target function T along different frequency directions.

Let us first consider (10). We have

$$\mathcal{F}_1[T](s, t) = \int e^{-i\omega(t-R_1(s,\mathbf{x})/c_0)} A_1(s, \mathbf{x}, \omega) T(\mathbf{x}) \, d\mathbf{x} \, d\omega \tag{35}$$

where $R_1(s, \mathbf{x}) = |\gamma_T(s) - \mathbf{x}| + |\mathbf{x} - \gamma_R(s)|$. For the sake of simplicity, let us assume that $A_{TR}(s, \mathbf{x}, \omega) \equiv 1$. Then, taking the temporal Fourier transform, we have

$$D_1(s, \omega) := \int e^{i\frac{\omega}{c_0} R_1(s,\mathbf{x})} T(\mathbf{x}) \, d\mathbf{x}. \tag{36}$$

Let us fix a point $\mathbf{x}_0 \in \mathbb{R}^2$ and expand $R_1(s, \mathbf{x})$ into a Taylor series centered at \mathbf{x}_0 :

$$R_1(s, \mathbf{x}) = R_1(s, \mathbf{x}_0) + (\mathbf{x} - \mathbf{x}_0) \left(\frac{\omega}{c_0} D(\mathbf{x}_0) (\widehat{\mathbf{x}_0 - \gamma_T(s)} + \widehat{\mathbf{x}_0 - \gamma_R(s)}) \right) + \dots \tag{37}$$

Then,

$$D_1(s, \omega) \approx e^{i\frac{\omega}{c_0} R_1(s,\mathbf{x}_0) - \mathbf{x}_0 \cdot \zeta_1} \widehat{T}(\zeta_1) \tag{38}$$

where

$$\zeta_1 = [D(\mathbf{x}_0)]^T \left(\frac{\omega}{c_0} (\widehat{\mathbf{x}_0 - \gamma_T(s)} + \widehat{\mathbf{x}_0 - \gamma_R(s)}) \right) \tag{39}$$

and \widehat{T} denotes the Fourier transform of T .

Similarly, from (11), (12) and (13), we obtain for $k = 2, 3$ and 4 ,

$$D_k(s, \omega) \approx e^{i\frac{\omega}{c_0} R_k(s,\mathbf{x}_0) - \mathbf{x}_0 \cdot \zeta_k} \widehat{T}(\zeta_k) \tag{40}$$

where ζ_k for $k = 2, 3$ and 4 are defined similar to (39) with $\{\gamma_T, \gamma_R\}$ in its definition replaced by $\{\tilde{\gamma}_T, \gamma_R\}$, $\{\gamma_T, \tilde{\gamma}_R\}$ and $\{\tilde{\gamma}_T, \tilde{\gamma}_R\}$, respectively. Recalling the definition of the data collection manifold from (30), we see from (38) and (40), that the data collection manifolds comprise of vectors in different directions. Therefore, in reconstructing T at the point \mathbf{x}_0 , by exploiting multi-path scattering, we have the Fourier transform of the target function T on a larger data collection manifold. Hence, backprojection of these measurements, in general, reconstructs edges with different orientation leading to an enhanced resolution.

4. Derivation of the backprojection filters

In this subsection, we describe the derivation of the backprojection filter B_j , $j = 1 \dots 4$. We design the backprojection filter B_j such that the MSE between the image (33) and the best possible image that could be reconstructed by the j th multi-path is minimized.

The data collection manifold given in (30) determines the best possible image that can be reconstructed by the j th multi-path when no *a priori* information is available outside the data collection manifold. This image is given by

$$T_{\Omega_z^j}(z) := \int_{\Omega_z^j} e^{i(x-z)\cdot\xi} T(x) \, dx \, d\xi. \tag{41}$$

We compute the filter B_j such that the MSE

$$I(B_j) = \int E[|\widehat{T}_j(z) - T_{\Omega_z^j}(z)|^2] \, dz \tag{42}$$

is minimized.

We now carry out the steps in the derivation of filter B_j . First, we substitute the expression (34) for \widehat{T}_j into (42) and obtain

$$I(B_j) = \int E[|(\mathcal{K}_j \mathcal{F}_j[T](z) - T_{\Omega_z^j}(z))|^2] \, dz \tag{43}$$

$$+ \int E \left[\left| \sum_{k=1, k \neq j}^4 \mathcal{K}_j \mathcal{F}_k[T](z) \right|^2 \right] \, dz \tag{44}$$

$$+ 2 \sum_{k=1, k \neq j}^4 \operatorname{Re} \int E[(\mathcal{K}_j \mathcal{F}_j[T](z) - T_{\Omega_z^j}(z)) \mathcal{K}_j \mathcal{F}_k[T](z)] \, dz \tag{45}$$

$$+ \int E[|\mathcal{K}_j n(z)|^2] \, dz. \tag{46}$$

Let us denote the four integrals (43)–(46) as I_1, I_2, I_3 and I_4 , respectively.

We simplify each of these integrals using the method of the stationary phase. In order to carry this out, we perform the following change of variables to transform the integral expressions of each of the summands on the right-hand side in (34):

$$(s, \omega) \rightarrow \xi = \frac{\omega}{c_0} \Sigma_j(x, z, s) \tag{47}$$

where

$$\Sigma_j(x, z, s) = \int_0^1 \nabla R_j(s, z + \lambda(x - z)) \, d\lambda \tag{48}$$

with ∇ denoting the gradient operator in the x variable. For $x = z$,

$$\Sigma_j(z, z, s) = [D(z_1, z_2)]^T ((\widehat{\tilde{\gamma}^m}(s) - z) + (\widehat{\tilde{\gamma}^n}(s) - z)), \tag{49}$$

where $D(z_1, z_2)$ is as in (31). In other words $\Sigma_j(z, z, s)$ is the projection of the bisector of $(\widehat{\tilde{\gamma}^m}(s) - z)$ and $(\widehat{\tilde{\gamma}^n}(s) - z)$ onto the tangent plane at z .

Then, writing

$$R_j(s, x) - R_j(s, z) = (x - z) \cdot \Sigma_j(x, z, s), \tag{50}$$

we obtain

$$\mathcal{K}_j \mathcal{F}_j(z) = \int e^{i(x-z)\cdot\xi} B_j(z, \xi) A_j(x, \xi) |J_j(x, z, \xi)| T(x) \, dx \, d\xi \tag{51}$$

where J_j is the determinant of the Jacobian of the inverse of the transformation in (47).

Using the change of variables, (47), in the remaining terms of (34), we obtain

$$\mathcal{K}_j \mathcal{F}_k(z) = \int e^{i(x-z)\cdot\xi} B_j(z, \xi) A_k(x, \xi) |J_j(x, z, \xi)| \tilde{T}_{jk}(x, \xi) dx d\xi \quad (52)$$

where

$$\tilde{T}_{jk}(x, \xi) := \tilde{T}_{jk}(x, s(\xi), \omega(\xi)) = e^{i\Delta_{jk}(x, s(\xi), \omega(\xi))} T(x) \quad (53)$$

and

$$\Delta_{jk}(x, s(\xi), \omega(\xi)) = \frac{\omega(\xi)}{c_0} (R_k(s(\xi), x) - R_j(s(\xi), x)). \quad (54)$$

Recall that R_k and R_j denote the total distance of the k th and j th multi-paths, respectively.

We now simplify the integrals $I_i, i = 1, \dots, 4$ using the method of stationary phase.

4.1. Calculation of I_1

We have

$$I_1 = \int \mathbb{E}[|(\mathcal{K}_j \mathcal{F}_j)[T](z) - T_{\Omega_j^i}(z)|^2] dz. \quad (55)$$

We show in appendix B that I_1 can be approximated as

$$I_1 \approx \int |B_j(x', \zeta) A_j(x', \zeta) J_j(x', x', \zeta) - 1|^2 S_T(\zeta) dx' d\zeta. \quad (56)$$

4.2. Calculation of I_2

We have

$$I_2 = \int \mathbb{E} \left[\left| \sum_{k=1, k \neq j}^4 \mathcal{K}_j \mathcal{F}_k[T](z) \right|^2 \right] dz. \quad (57)$$

We show in appendix C that I_2 can be approximated as

$$I_2 \approx \sum_{k=1, k \neq j}^4 \int |A_k(x', \zeta) B_j(x', \zeta) J_j(x', x', \zeta)|^2 S_T(\zeta + \partial_{x'} \Delta_{jk}(0, \zeta)) dx' d\zeta. \quad (58)$$

4.3. Calculation of I_3

We show in appendix D that with the assumption of stationarity of T , the leading-order contribution of I_3 to $I(B_j)$ is 0. Therefore, this integral does not contribute to the determination of the filter B_j .

4.4. Calculation of I_4

We have

$$I_4 = \int \mathbb{E}[|\mathcal{K}[n](z)|^2] dz \quad (59)$$

$$= \int e^{i(\frac{\omega'}{c_0} R_j(s', z) - \frac{\omega}{c_0} R_j(s, z))} B_j(z, s, \omega) \overline{B_j(z, s', \omega')} \tilde{S}_n(s, \omega, s', \omega') ds ds' d\omega d\omega' dz. \quad (60)$$

With condition (25), we obtain

$$I_4 = \int |B_j(z, s, \omega)|^2 S_n(s, \omega) d\omega ds dz. \quad (61)$$

Making the change of variables (47) in this integral, we have

$$I_4 = \int |B_j(z, \zeta)|^2 S_n(\zeta) |J(z, z, \zeta)| dz d\zeta. \quad (62)$$

The contributions to $I(B_j)$ are

$$I(B_j) \approx I_1 + I_2 + I_4, \quad (63)$$

where I_1 , I_2 and I_4 are given by (55), (58) and (62), respectively. We wish to choose the filter B_j such that $I(B_j)$ is minimum.

4.5. Variational derivative of MSE with respect to B_j

We consider the variational derivative to minimize I with respect to B_j . That is, we fix a filter B_0 and consider the variation, $B_j + \varepsilon B_0$ for small ε . If B_j is such that $I(B_j)$ is a minimum, we must have

$$\frac{d}{d\varepsilon} I(B_j + \varepsilon B_0)|_{\varepsilon=0} = 0. \quad (64)$$

Equation (64) must hold for any B_0 and so varying B_0 leads to the determination of the filter B_j . These steps are carried out in appendix E. The optimal filter satisfying (64) is given by

$$B_j(\mathbf{x}, \zeta) = \frac{\chi_{\Omega_x^j} \overline{A_j(\mathbf{x}, \zeta)} S_T(\zeta)}{\Psi} \quad (65)$$

where

$$\Psi = |J_j(\mathbf{x}, \mathbf{x}, \zeta)| \left\{ |A_j(\mathbf{x}, \zeta)|^2 S_T(\zeta) + \sum_{k=1, k \neq j}^4 |A_k(\mathbf{x}, \zeta)|^2 S_T(\zeta + \partial_x \Delta_{jk}(0, \zeta)) \right\} + S_n(\zeta), \quad \zeta \in \Omega_x^j. \quad (66)$$

Here $\chi_{\Omega_x^j}$ is the characteristic function equal to 1 on the data collection manifold (30) and zero everywhere else, and Δ_{jk} is given in (54).

We now write filter (65) as a function of \mathbf{x} , s and ω . We simplify further by making the assumption that the size of the target scene is much smaller as compared to the distance of the airborne platforms from the target scene. Note that this assumption is realistic for SAR imaging scenarios.

We then have,

$$\zeta + \partial_x \Delta_{jk}(0, \zeta) \approx \zeta_k$$

where ζ_1 is defined as in (39):

$$\zeta_1 = [D(x_1, x_2)]^T \left(\frac{\omega}{c_0} (\mathbf{x}_0 - \widehat{\gamma}_T(s) + \mathbf{x}_0 - \widehat{\gamma}_R(s)) \right) \quad (67)$$

and ζ_k , $k = 2, 3$ and 4 are defined with $\{\gamma_T, \gamma_R\}$ in (67) replaced by $\{\tilde{\gamma}_T, \gamma_R\}$, $\{\gamma_T, \tilde{\gamma}_R\}$ and $\{\tilde{\gamma}_T, \tilde{\gamma}_R\}$, respectively.

This follows because, ζ in the variable (s, ω) is

$$\zeta = \frac{\omega}{c_0} [D(x_1, x_2)]^T (\mathbf{x} - \widehat{\gamma}_T(s) + \mathbf{x} - \widehat{\tilde{\gamma}}_R(s)) \quad (68)$$

and for small variations of \mathbf{x} from the origin, we have that the unit vectors $\widehat{\mathbf{x}} - \widehat{\gamma_T}(s)$, $\widehat{\mathbf{x}} - \widehat{\tilde{\gamma}_T}(s)$, $\widehat{\mathbf{x}} - \widehat{\gamma_R}(s)$, $\widehat{\mathbf{x}} - \widehat{\tilde{\gamma}_R}(s)$ have small variation in directions from that of $\widehat{\psi_0} - \widehat{\gamma_T}(s)$, $\widehat{\psi_0} - \widehat{\tilde{\gamma}_T}(s)$, $\widehat{\psi_0} - \widehat{\gamma_R}(s)$, $\widehat{\psi_0} - \widehat{\tilde{\gamma}_R}(s)$, respectively with $\psi_0 = (0, 0, \psi(0, 0))$. Hence,

$$B_j(\mathbf{x}, s, \omega) \approx \frac{\chi_{\Omega_x^j}(\mathbf{x}, s, \omega) \overline{A_j(\mathbf{x}, s, \omega)} S_T(\zeta)}{\Psi} \quad (69)$$

where

$$\Psi = |J_j(\mathbf{x}, \mathbf{x}, s, \omega)| \sum_{k=1}^4 |A_k(\mathbf{x}, s, \omega)|^2 S_T(\zeta_k) + S_n(\zeta) \quad (70)$$

where ζ is defined in (68) and ζ_k are defined similar to (67).

4.6. Reconstructed image

In the previous subsections, we derived the filter B_j for the FBP operator \mathcal{K}_j and obtained the image \widehat{T}_j . Similarly, we can derive the filters corresponding to all other paths and obtain the final image by a coherent superposition of all the images:

$$\widehat{T}(z) := \sum_{j=1}^4 \widehat{T}_j(z). \quad (71)$$

5. Numerical simulations

In our numerical simulations, we considered a scene of size $[0, 22] \times [0, 22]$ km² discretized to a 168×168 grid of pixels with (0, 0) and (22, 22) corresponding to pixel numbers (1, 1) and (168, 168), respectively. Therefore, each pixel is approximately 131×131 m² in size. The target consists of an L-shaped object, such as the corner of a building, as shown in figure 3(a). We label the L-shaped object into two parts: Edge 1 and Edge 2. Edge 1 is at an inclination of 30° to the x -axis in the counterclockwise direction, while Edge 2 is at an inclination of 30° to the y -axis in the counterclockwise direction as shown in figure 3(a). Note that the gradients of the target at these edges are perpendicular to each other. The cross section of the perfectly reflecting vertical wall which is parallel to the y -axis and perpendicular to the scene is shown by the red vertical line in figure 3(a).

A stationary transmitter is located at $\gamma_T(s) \equiv [18, 18, 6.5]$ and a mobile receiver traverses a semi-circular trajectory $\gamma_R(s)$ of radius 11 km centered at (11, 11) and at a constant height of 6.5 km above the target scene: $\gamma_R(s) = [11 + 11 \sin s, 11 - 11 \cos s, 6.5]$ for $0 \leq s \leq \pi$. The location of the virtual stationary transmitter obtained by reflection about the vertical wall is then $\tilde{\gamma}_T(s) \equiv [4, 18, 6.5]$ and the trajectory of the virtual receiver is $\tilde{\gamma}_R(s) = [11 - 11 \sin s, 11 - 11 \cos s, 6.5]$ for $0 \leq s \leq \pi$ (see figure 3(b)).

We made the assumptions that the Earth's surface is flat and the amplitude functions $A_i \equiv 1$ for $i = 1, \dots, 4$. This choice of amplitude functions corresponds to isotropic transmitters and receivers using a delta function as the transmit waveforms. The parameters we used correspond to an effective system bandwidth of approximately 1.15 MHz.

The computational complexity of our method is based on three steps in the image formation algorithm: computing the Fourier transform of the data in the fast-time variable t , filtering in the Fourier domain, and finally, backprojection.

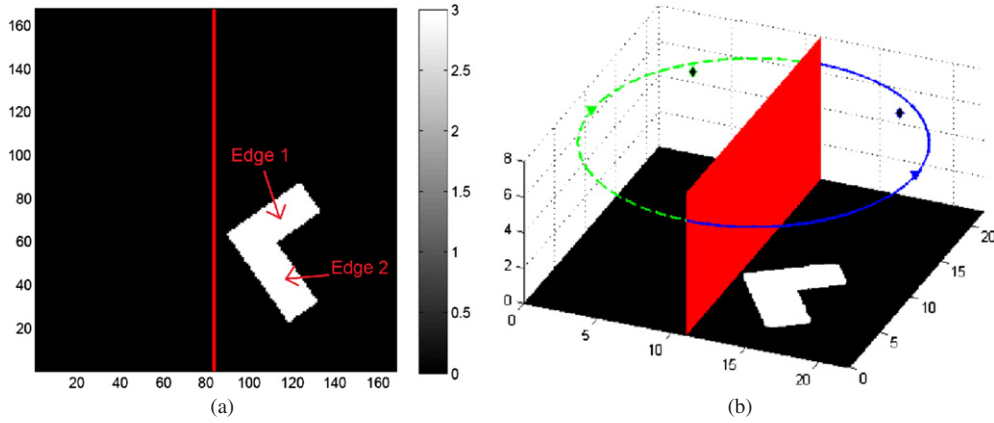


Figure 3. (a) Scene used in numerical simulations. The upper edge at an inclination of 30° to the x -axis in the counterclockwise direction is denoted as Edge 1, while the lower edge at an inclination of 30° to the y -axis in the counterclockwise direction is denoted as Edge 2. The red vertical line shows the cross section of the wall. (b) Three-dimensional view of the target scene and the vertical wall. The location of the stationary transmitter is indicated by the diamond to the right of the wall and the trajectory of the transmitter is given by the solid blue line on the right-hand side of the wall. The dotted trajectory and the diamond on the left-hand side of the wall are the reflected trajectory and the reflection location of the receiver and transmitter respectively.

The Fourier transform of the data in the fast-time variable is

$$D(s, \omega) = \int e^{i\omega t} d(s, t) dt. \quad (72)$$

Assume that there are $\mathcal{O}(N)$ samples in both fast-time and slow-time variables, for each fixed slow-time s , the Fourier transform of the fast-time variable t in (72) can be computed using the fast Fourier transform. This has a computational complexity of $\mathcal{O}(N \log N)$. Hence, over all s , the computational complexity is $\mathcal{O}(N^2 \log N)$.

Next, in the filtering step, we perform,

$$D_{B_j}(\mathbf{x}, s, \omega) = D(s, \omega) B_j(\mathbf{x}, s, \omega). \quad (73)$$

Assuming the image is of size $\mathcal{O}(N \times N)$, the filtering step (73) requires $\mathcal{O}(N^4)$ operations.

Finally, the backprojection step is

$$\hat{T}_j(\mathbf{z}) = \int e^{i\frac{\omega}{c_0} R_j(s, \mathbf{z})} D_{B_j}(\mathbf{z}, s, \omega) d\omega ds. \quad (74)$$

This step requires $\mathcal{O}(N^4)$ operations, as we perform this step by multiplication and then integration.

Hence, the computational complexity of our image reconstruction method requires $\mathcal{O}(N^4)$ operations. However, nowadays, filtered backprojection techniques can easily be implemented on graphic cards, with significant benefits in terms of computing speed [1].

Our first set of simulations in figure 4 show that taking into account multi-paths can lead to increased resolution. For this, we assumed that the received data can be isolated into components corresponding to the four multi-paths. For each of these four components, we used the bi-static FBP algorithm described in [22] to reconstruct the images. Figure 4(a) shows the image reconstructed by the data due to the path, Transmitter \rightarrow Target \rightarrow Receiver. This

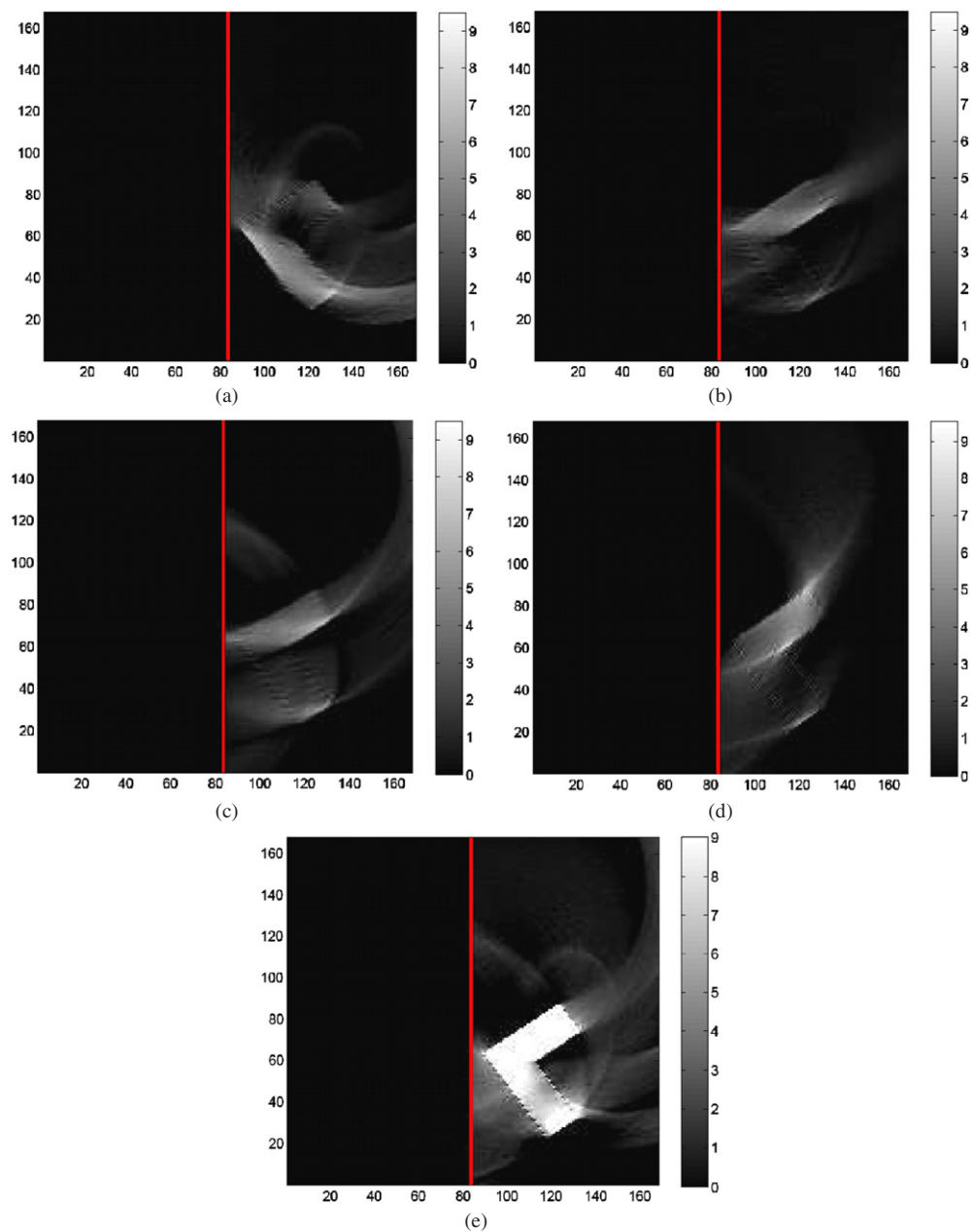


Figure 4. The images reconstructed by the bi-static FBP algorithm of [22] assuming that the received data can be separated according to each multi-path. Image reconstructed when the received data is modeled based on the following. (a) Direct bi-static path, Transmitter \rightarrow Target \rightarrow Receiver. (b) Multi-path, Transmitter \rightarrow Wall \rightarrow Target \rightarrow Receiver. Note that this is equivalent to the bi-static path, Virtual Transmitter \rightarrow Target \rightarrow Receiver. (c) Multi-path, Transmitter \rightarrow Target \rightarrow Wall \rightarrow Receiver. This multi-path is equivalent to the bi-static path, Transmitter \rightarrow Target \rightarrow Virtual Receiver. (d) Multi-path, Transmitter \rightarrow Wall \rightarrow Target \rightarrow Wall \rightarrow Receiver. This multi-path is equivalent to the bi-static path, Virtual Transmitter \rightarrow Target \rightarrow Virtual Receiver. (e) Superposition of the images reconstructed in (a), (b), (c) and (d).

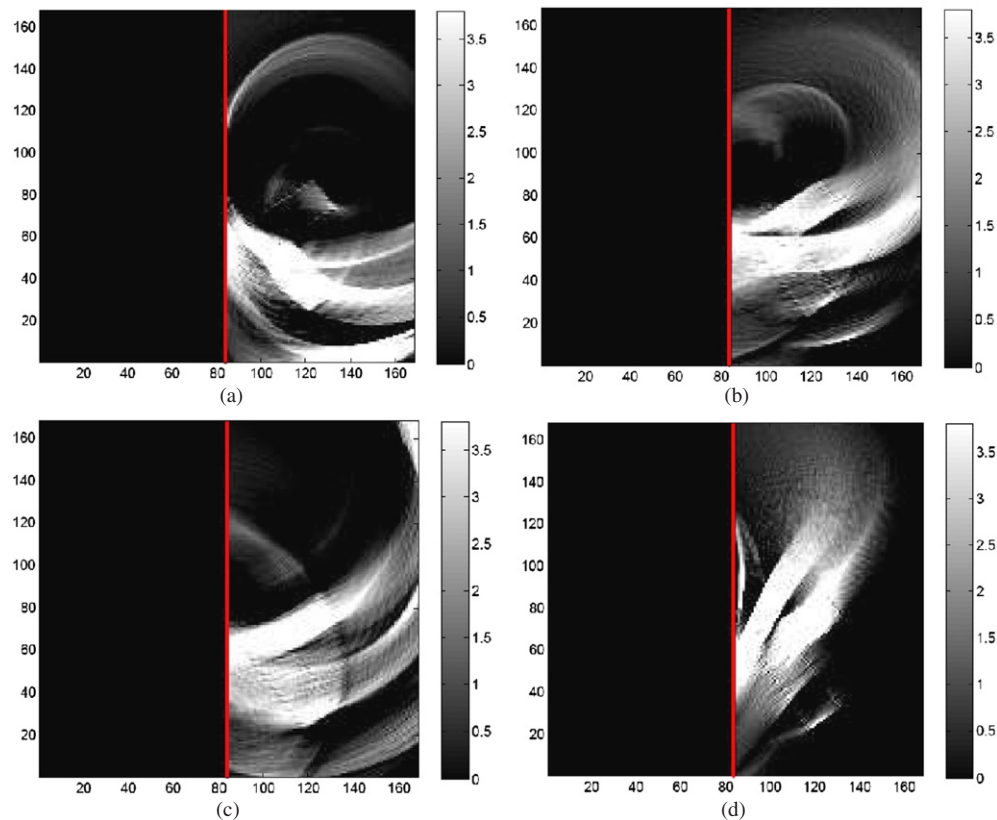


Figure 5. The images reconstructed by the bi-static FBP algorithm of [22] assuming that the received data *cannot* be separated into components corresponding to each multi-path. Image reconstructed by filtered-backprojection with respect to the following. (a) Direct bi-static path, Transmitter \rightarrow Target \rightarrow Receiver. (b) Multi-path, Transmitter \rightarrow Wall \rightarrow Target \rightarrow Receiver. Note that this is equivalent to the bi-static path, Virtual Transmitter \rightarrow Target \rightarrow Receiver. (c) Multi-path, Transmitter \rightarrow Target \rightarrow Wall \rightarrow Receiver. This multi-path is equivalent to the bi-static path, Transmitter \rightarrow Target \rightarrow Virtual Receiver. (d) Multi-path, Transmitter \rightarrow Wall \rightarrow Target \rightarrow Wall \rightarrow Receiver. This multi-path is equivalent to the bi-static path, Virtual Transmitter \rightarrow Target \rightarrow Virtual Receiver.

data reconstructs Edge 2, but not Edge 1. On the other hand, the data due to the other paths, Transmitter \rightarrow Target \rightarrow Wall \rightarrow Receiver, Transmitter \rightarrow Wall \rightarrow Target \rightarrow Receiver, and Transmitter \rightarrow Wall \rightarrow Target \rightarrow Wall \rightarrow Receiver, reconstruct Edge 1. These images are shown in figures 4(b)–(d), respectively. Finally, the superposition of the four reconstructed images in figure 4(e) shows that all edges are visible.

In the second set of simulations, shown in figure 5, we made the assumption that we cannot isolate the received data into components corresponding to the different scattering paths. We used the bi-static FBP algorithm of [22] to reconstruct the images. In comparing the four images of figure 5 with the corresponding four images of figure 4, we see that, while the bi-static FBP algorithm of [22] reconstructs additional edges of the target, artifacts are created due to not being able to decompose the received data into components due to each multi-path.

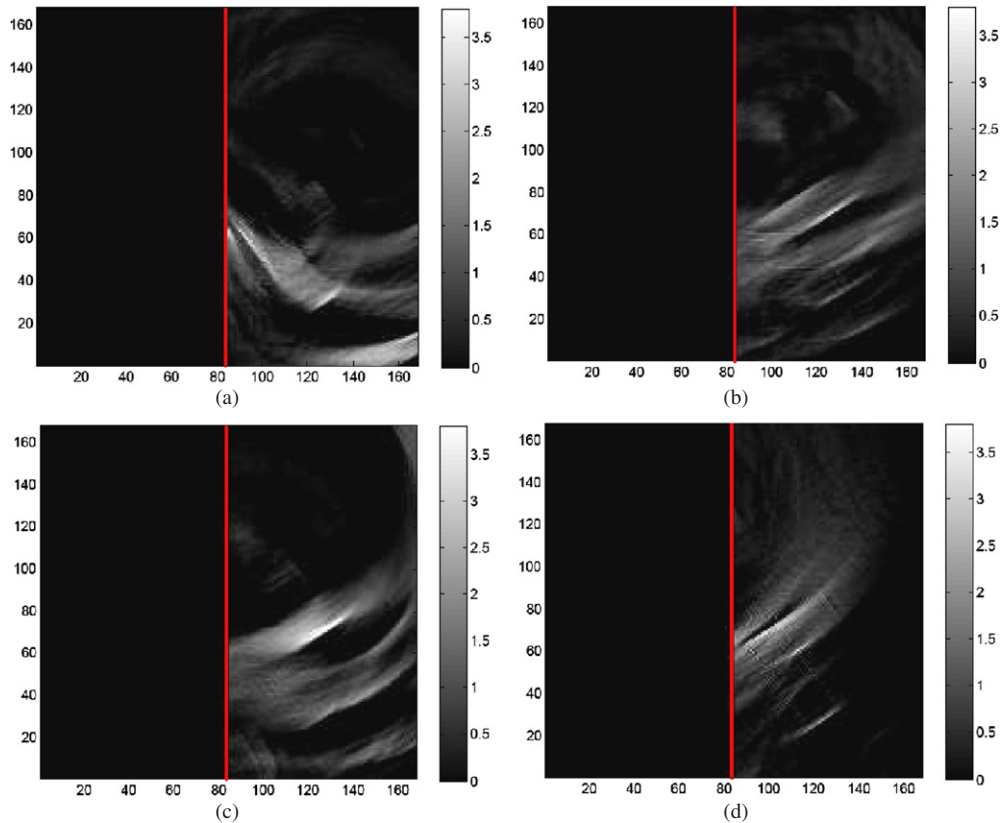


Figure 6. The images reconstructed by the algorithm developed in this paper. Image reconstructed by the multi-path filtered-backprojection with respect to the following. (a) Direct bi-static path, Transmitter \rightarrow Target \rightarrow Receiver. (b) Multi-path, Transmitter \rightarrow Wall \rightarrow Target \rightarrow Receiver. Note that this is equivalent to the bi-static path, Virtual Transmitter \rightarrow Target \rightarrow Receiver. (c) Multi-path, Transmitter \rightarrow Target \rightarrow Wall \rightarrow Receiver. This multi-path is equivalent to the bi-static path, Transmitter \rightarrow Target \rightarrow Virtual Receiver. (d) Multi-path, Transmitter \rightarrow Wall \rightarrow Target \rightarrow Receiver. This multi-path is equivalent to the bi-static path, Virtual Transmitter \rightarrow Target \rightarrow Virtual Receiver.

Our third set of simulations in figure 6 shows that the artifacts created by using the bi-static FBP algorithm of [22] with the multi-path data can be suppressed. For this, we used the multi-path reconstruction algorithm developed in this paper to reconstruct the images. Comparing the four images in figure 6 with the corresponding images in figure 5, we see that the filters developed in this paper suppresses the strength of the artifacts created when the bi-static FBP algorithm of [22] is employed to multi-path data.

In figure 7, we compared the superposition of the four images of figure 5 with the superposition of the four images of figure 6. We see that the reconstruction algorithm introduced in this paper is able to reconstruct the image and at the same time reduce the strength of the artifacts induced by the backprojection algorithm of [3, 22].

Finally, we performed a simulation where the multi-path data is corrupted with noise. Since the transmitted pulse is an ideal wide-band signal, we chose a wide-band noise model

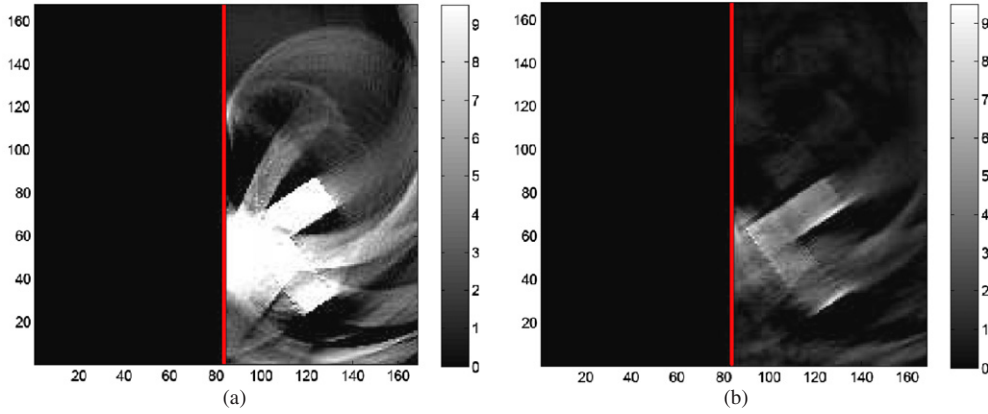


Figure 7. (a) Coherent superposition of the images reconstructed by the bi-static FBP algorithm of [22] for each multi-path. (b) Coherent superposition of the images reconstructed by the multi-path algorithm of this paper.

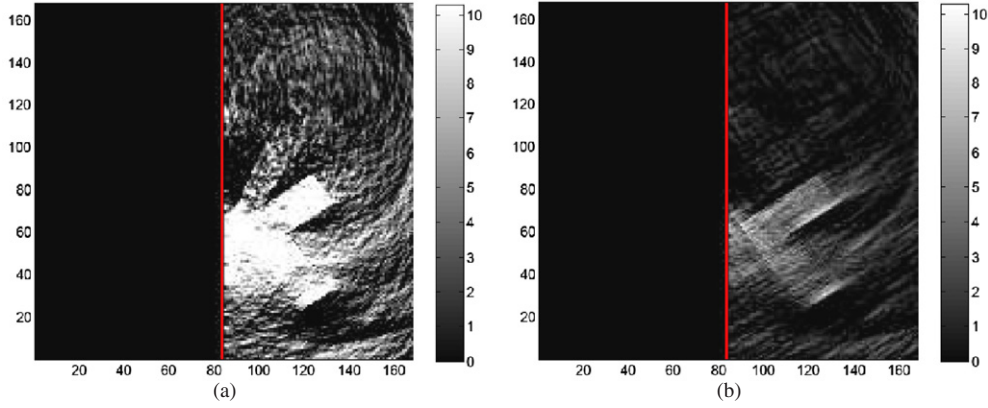


Figure 8. Multi-path imaging set-up with data at the receiver corrupted with noise at SNR of 5 dB. (a) Coherent superposition of the images reconstructed by the bi-static FBP algorithm of [22] for each multi-path. (b) Coherent superposition of the images reconstructed by the multi-path algorithm of this paper.

which behaves like a $1/f$ -type noise process:

$$S_n(s, \omega) = \frac{1}{1 + |\omega|^5} \frac{\pi/5}{\sin(\pi/5)}. \quad (75)$$

We define the signal-to-noise ratio as

$$\text{SNR} = 20 \log \frac{\frac{1}{N_d} \sum_{i=1}^{N_d} (d(s_i, t_i) - \mu_d)^2}{E[\|n\|^2]} \text{dB}, \quad (76)$$

where N_d is the number of grid points and μ_d is the mean value of the received data.

Figure 8 compares the image reconstructed by the bi-static FBP algorithm of [3, 22] and the multi-path algorithm of this paper when the received data is corrupted with noise at $\text{SNR} = 5$ dB. Visual comparison of the images in figures 8(a) and (b) shows the suppression of artifacts due to noise when the filter in this paper is used, as compared to the filter in [22].

6. Conclusions and future developments

In this paper, we developed an FBP-type inversion method for SAR imaging in a multiple scattering environment. We assumed that a bi-static SAR system is used in imaging a target of interest located in the vicinity of a perfectly reflecting vertical wall. We considered a ray theoretic approximation to the Green function and took into account the different scattering paths that interact with the target once.

The received signals from the different scattering paths and additive noise may interfere, leading to artifacts in the reconstructed images. Under the assumption that we have *a priori* knowledge of the power spectral density function of the target and the additive thermal noise, we developed an FBP-type imaging algorithm that reconstructs the image of the target while suppressing the artifacts caused by interference due to multiple scattering paths and thermal noise.

In this paper, we assumed that the target is composed of isotropic scatterers. Our image formation method can be generalized to the case where there are multiple transmitters and receivers. We give the main ideas involved in generalizing our multi-path image formation method for a multi-static scenario involving multiple transmitters and receivers used in imaging a target adjacent to a perfectly reflecting vertical wall. Let us assume that M transmitters and N receivers are involved in imaging the target. The received data at the q th receiver for $q = 1, \dots, N$ is the superposition of the multi-path data (14) due to each of the M transmitters and the additive thermal noise at this receiver. We then use the image formation technique of section 3 to derive a filter for each of the transmitter–receiver, virtual transmitter–receiver, transmitter–virtual receiver and virtual transmitter–virtual receiver pairs. The final image is then obtained as a coherent superposition of these reconstructed images.

In developing our image formation method, we assumed that the target to be imaged is composed of isotropic scatterers. This assumption simplifies the derivation of the image formation algorithm. However, the assumption of isotropic scatterers is only valid for small aperture angles [12, 15]. Bi-static SAR systems are capable of forming large aperture angles, and hence the assumption that target is composed of isotropic scatterers may not be valid. In our work [13, section V], based on the approach of [12], we developed an image formation method for a target composed of anisotropic scatterers in a multi-static setting. The same ideas, with suitable modifications, can be carried over to our multiple scattering scenario.

The present work required *a priori* knowledge of the known background scatterer (the wall). Specifically, we required knowledge of its location, size and reflection parameter. In the case where such *a priori* information is not available, we have to consider an autofocus-like problem as the phase functions in (15) will have errors causing the reconstructed images to be improperly focused. A first step to deal with such a problem is to consider the phase function in (15) to be a random process in addition to the target reflectivity function. We plan to address this in our future work.

In this paper, we derived the data model ((10)–(13)) based on the scalar wave equation and making the assumption of single scattering Born approximation. Therefore, polarization is not built into our data model and our imaging method cannot predict polarization related effects. If polarization is to be considered, then one has to derive a data model using the vector wave equation. In that case, the target is modeled as a 3×3 matrix of functions instead of a single reflectivity function. The imaging algorithm then has to recover these nine functions. We expect the polarization diverse imaging method and associated analysis to be significantly more complicated than the scalar case. We plan to address this in our future work.

Finally, while our paper has focused primarily on image formation in a radar setting, the techniques are also applicable to other imaging problems such as those arising in acoustics, geophysics and tomography.

Acknowledgments

Both authors were supported in part by AFOSR under the agreements FA9550-07-1-0363, FA9550-09-1-0013 and in part by NSF grant CCF-08030672. The first author was supported in part by NSF grant DMS-1028096 which was a supplement to Eric Todd Quinto’s NSF grant DMS-0908015.

Appendix A. Method of the stationary phase

Let u be a smooth function of compact support in \mathbb{R}^n and let φ be a real valued function with only non-degenerate critical points. A point $x_0 \in \mathbb{R}^n$ is called a non-degenerate critical point if $D\varphi(x_0) = 0$ and the Hessian matrix $D^2\varphi(x_0)$ has non-zero determinant. The stationary phase theorem states as $\lambda \rightarrow \infty$

$$\int e^{i\lambda\varphi(x)} u(x) dx = \left(\frac{2\pi}{\lambda}\right)^{n/2} \sum_{\{x_0: D\varphi(x_0)=0\}} \frac{e^{i\lambda\varphi(x_0)} e^{i\pi/4 \text{Sgn} D^2\varphi(x_0)}}{\sqrt{|\det D^2\varphi(x_0)|}} + \mathcal{O}(\lambda^{-n/2-1}). \tag{A.1}$$

Appendix B. The stationary phase calculation of I_1

We have

$$I_1 = I_1 = \int E[|\mathcal{K}_j \mathcal{F}_j[T](z) - T_{\Omega'_z}(z)|^2] dz = \int e^{i((x-z)\cdot\xi - (x'-z)\cdot\xi')} (B_j(z, \xi) A_j(x, \xi) |J_j(x, z, \xi)| - 1) \tag{B.1}$$

$$\times \overline{(B_j(z, \xi') A_j(x', \xi') |J_j(x', z, \xi')| - 1)} R_T(x, x') dx dx' d\xi d\xi' dz. \tag{B.2}$$

We apply the method of the stationary phase in the variables z and ξ' . We denote the phase function

$$\varphi_1(x, x', z, \xi, \xi') = (x - z) \cdot \xi - (x' - z) \cdot \xi'. \tag{B.3}$$

Differentiating φ_1 with respect to z and ξ' and setting it equal to 0, we have the critical points at

$$\xi' = \xi \quad \text{and} \quad z = x'. \tag{B.4}$$

Now by the method of the stationary phase, we obtain

$$I_1 \approx \int e^{i(x-x')\cdot\xi} (B_j(x', \xi) A_j(x, \xi) |J_j(x, x', \xi)| - 1) \times \overline{(B_j(x', \xi) A_j(x', \xi) |J_j(x', x', \xi)| - 1)} R_T(x, x') dx dx' d\xi. \tag{B.5}$$

Writing

$$R_T(x, x') = \int e^{-i(x\cdot\zeta - x'\cdot\zeta')} \tilde{S}_T(\zeta, \zeta') d\zeta d\zeta', \tag{B.6}$$

we obtain

$$I_1 \approx \int e^{i((x-x')\cdot\xi - x\cdot\zeta + x'\cdot\zeta')} (B_j(x', \xi) A_j(x, \xi) |J_j(x, x', \xi) - 1| \times \overline{(B_j(x', \xi) A_j(x', \xi) |J_j(x', x', \xi) - 1|)} \widetilde{S}_T(\zeta, \zeta') dx dx' d\xi d\zeta d\zeta'. \quad (B.7)$$

We now apply the method of the stationary phase in the variables, x and ξ . We denote the phase function

$$\varphi_2(x, x', \zeta, \zeta', \xi) = (x - x') \cdot \xi - x \cdot \zeta + x' \cdot \zeta'. \quad (B.8)$$

Differentiate φ_2 with respect to x and ξ and set it to equal to 0 to obtain the critical points

$$\xi = \zeta \quad \text{and} \quad x = x'. \quad (B.9)$$

Again by the method of the stationary phase we have

$$I_1 \approx \int e^{ix'\cdot(\zeta' - \zeta)} |B_j(x', \zeta) A_j(x', \zeta) |J_j(x', x', \zeta) - 1|^2 \widetilde{S}_T(\zeta, \zeta') dx' d\zeta d\zeta'. \quad (B.10)$$

Assuming stationarity of S_T , we have

$$I_1 \approx \int |B_j(x', \zeta) A_j(x', \zeta) |J_j(x', x', \zeta) - 1|^2 S_T(\zeta) dx' d\zeta. \quad (B.11)$$

Appendix C. The stationary phase calculation of I_2

Consider

$$I_2 = \int E \left[\left| \sum_{k=1, k \neq j}^4 \mathcal{K}_j \mathcal{F}_k [T](z) \right|^2 \right] dz \quad (C.1)$$

Expanding the right-hand side we obtain

$$I_2 = \sum_{k,l=1, k,l \neq j}^4 \int e^{i[(x-z)\cdot\xi - (x'-z)\cdot\xi']} B_j(z, \xi) A_k(x, \xi) |J_j(x, z, \xi)| \times \overline{B_j(z, \xi') A_l(z, \xi') |J_j(x, z, \xi')|} e^{i(\Delta_{jk}(x, \xi) - \Delta_{jl}(x', \xi'))} R_T(x, x') dx dx' d\xi d\xi' dz \quad (C.2)$$

where Δ_{jk} is given by (54) and Δ_{jl} is defined similarly.

Now we obtain a simplified expression for

$$e^{i(\Delta_{jk}(x, \xi) - \Delta_{jl}(x', \xi'))} R_T(x, x'). \quad (C.3)$$

To do so we first expand $\Delta_{jk}(\cdot, \xi)$ and $\Delta_{jl}(\cdot, \xi')$ near the origin:

$$\Delta_{jk}(x, \xi) = \Delta_{jk}(0, \xi) + x \cdot \frac{\partial}{\partial x} \Delta_{jk}(0, \xi) + \text{higher order terms}, \quad (C.4)$$

$$\Delta_{jl}(x', \xi') = \Delta_{jl}(0, \xi') + x' \cdot \frac{\partial}{\partial x'} \Delta_{jl}(0, \xi') + \text{higher order terms}. \quad (C.5)$$

We make the assumption that for all k, l , at the origin, $\Delta_{jk}(0, \xi) \approx 0$ and $\Delta_{jl}(0, \xi') \approx 0$ and neglect the higher order terms in these Taylor series expansions.

By the Fourier inversion formula, we have from (22),

$$R_T(x, x') = \int e^{-i(x\cdot\zeta - x'\cdot\zeta')} \widetilde{S}_T(\zeta, \zeta') d\zeta d\zeta'. \quad (C.6)$$

Therefore, we obtain

$$e^{i(\Delta_{jk}(\mathbf{x}, \boldsymbol{\xi}) - \Delta_{jl}(\mathbf{x}', \boldsymbol{\xi}'))} R_T(\mathbf{x}, \mathbf{x}') \approx \int e^{-i(\mathbf{x} \cdot \boldsymbol{\zeta} - \mathbf{x}' \cdot \boldsymbol{\zeta}')} \tilde{S}_T(\boldsymbol{\zeta} + \partial_{\mathbf{x}} \Delta_{jk}(0, \boldsymbol{\xi}), \boldsymbol{\zeta}' + \partial_{\mathbf{x}'} \Delta_{jl}(0, \boldsymbol{\xi}')) d\boldsymbol{\zeta} d\boldsymbol{\zeta}'. \quad (\text{C.7})$$

Substituting this back into (C.2), we obtain

$$I_2 \approx \sum_{k,l=1,k,l \neq j}^4 \int e^{i[(\mathbf{x}-\mathbf{z}) \cdot \boldsymbol{\xi} - (\mathbf{x}'-\mathbf{z}) \cdot \boldsymbol{\xi}' - (\mathbf{x} \cdot \boldsymbol{\zeta} - \mathbf{x}' \cdot \boldsymbol{\zeta}')] } B_j(\mathbf{z}, \boldsymbol{\xi}) A_k(\mathbf{x}, \boldsymbol{\xi}) |J_j(\mathbf{x}, \mathbf{z}, \boldsymbol{\xi})| \\ \times \overline{B_j(\mathbf{z}, \boldsymbol{\xi}') A_l(\mathbf{z}, \boldsymbol{\xi}') |J_j(\mathbf{x}, \mathbf{z}, \boldsymbol{\xi}')|} \tilde{S}_T(\boldsymbol{\zeta} + \partial_{\mathbf{x}} \Delta_{jk}(0, \boldsymbol{\xi}), \boldsymbol{\zeta}' \\ + \partial_{\mathbf{x}'} \Delta_{jl}(0, \boldsymbol{\xi}')) d\mathbf{x} d\mathbf{x}' d\boldsymbol{\xi} d\boldsymbol{\xi}' dz. \quad (\text{C.8})$$

We now apply the method of the stationary phase to this integral. Denote the phase function,

$$\varphi_3(\mathbf{x}, \mathbf{x}', \boldsymbol{\xi}, \boldsymbol{\xi}', \boldsymbol{\zeta}, \boldsymbol{\zeta}') = (\mathbf{x} - \mathbf{z}) \cdot \boldsymbol{\xi} - (\mathbf{x}' - \mathbf{z}) \cdot \boldsymbol{\xi}' - \mathbf{x} \cdot \boldsymbol{\zeta} + \mathbf{x}' \cdot \boldsymbol{\zeta}'. \quad (\text{C.9})$$

We compute the derivatives of φ_3 with respect to \mathbf{z} , $\boldsymbol{\xi}'$, \mathbf{x} , $\boldsymbol{\xi}$ and set it equal to 0. We obtain the following:

$$\boldsymbol{\xi}' = \boldsymbol{\xi}, \quad \boldsymbol{\xi} = \boldsymbol{\zeta}, \quad \mathbf{z} = \mathbf{x}', \quad \mathbf{x} = \mathbf{x}'. \quad (\text{C.10})$$

Hence, by the method of the stationary phase, we have the following integral representation:

$$I_2 \approx \sum_{k,l \in \text{paths}, k,l \neq j, j^{\text{sym}}} \int e^{i\mathbf{x}' \cdot (\boldsymbol{\zeta}' - \boldsymbol{\zeta})} |A_k(\mathbf{x}', \boldsymbol{\zeta}) B_j(\mathbf{x}', \boldsymbol{\zeta}) J_j(\mathbf{x}', \mathbf{x}', \boldsymbol{\zeta})|^2 \\ \times \tilde{S}_T(\boldsymbol{\zeta} + \partial_{\mathbf{x}'} \Delta_{jk}(0, \boldsymbol{\zeta}), \boldsymbol{\zeta}' + \partial_{\mathbf{x}'} \Delta_{jl}(0, \boldsymbol{\zeta})) d\mathbf{x}' d\boldsymbol{\zeta} d\boldsymbol{\zeta}' \quad (\text{C.11})$$

$$+ \sum_{k,l=1,k,l \neq j}^4 \int e^{i\mathbf{x}' \cdot (\boldsymbol{\zeta}' - \boldsymbol{\zeta})} A_k(\mathbf{x}', \boldsymbol{\zeta}) \overline{A_l(\mathbf{x}', \boldsymbol{\zeta})} |B_j(\mathbf{x}', \boldsymbol{\zeta}) J_j(\mathbf{x}', \mathbf{x}', \boldsymbol{\zeta})|^2 \\ \times \tilde{S}_T(\boldsymbol{\zeta} + \partial_{\mathbf{x}'} \Delta_{jk}(0, \boldsymbol{\zeta}), \boldsymbol{\zeta}' + \partial_{\mathbf{x}'} \Delta_{jl}(0, \boldsymbol{\zeta})) d\mathbf{x}' d\boldsymbol{\zeta} d\boldsymbol{\zeta}'. \quad (\text{C.12})$$

We observe that in the integral expression

$$\sum_{k,l=1,k,l \neq j}^4 \int e^{i\mathbf{x}' \cdot (\boldsymbol{\zeta}' - \boldsymbol{\zeta})} A_k(\mathbf{x}', \boldsymbol{\zeta}) \overline{A_l(\mathbf{x}', \boldsymbol{\zeta})} |B_j(\mathbf{x}', \boldsymbol{\zeta}) J_j(\mathbf{x}', \mathbf{x}', \boldsymbol{\zeta})|^2 \\ \times \tilde{S}_T(\boldsymbol{\zeta} + \partial_{\mathbf{x}'} \Delta_{jk}(0, \boldsymbol{\zeta}), \boldsymbol{\zeta}' + \partial_{\mathbf{x}'} \Delta_{jl}(0, \boldsymbol{\zeta})) d\mathbf{x}' d\boldsymbol{\zeta} d\boldsymbol{\zeta}', \quad (\text{C.13})$$

the leading-order contribution is when $\boldsymbol{\zeta} = \boldsymbol{\zeta}'$ because of the oscillatory term $e^{i\mathbf{x}' \cdot (\boldsymbol{\zeta} - \boldsymbol{\zeta}')}$. When $\boldsymbol{\zeta} = \boldsymbol{\zeta}'$, we have

$$\tilde{S}_T(\boldsymbol{\zeta} + \partial_{\mathbf{x}'} \Delta_{jk}(0, \boldsymbol{\zeta}), \boldsymbol{\zeta} + \partial_{\mathbf{x}'} \Delta_{jl}(0, \boldsymbol{\zeta})) = 0 \quad (\text{C.14})$$

by the stationarity assumption. Therefore, this integral expression does not have any leading-order contribution to I_2 . Furthermore, by stationarity of S_T , we obtain

$$I_2 \approx \sum_{k=1,k \neq j}^4 \int |A_k(\mathbf{x}', \boldsymbol{\zeta}) B_j(\mathbf{x}', \boldsymbol{\zeta}) J_j(\mathbf{x}', \mathbf{x}', \boldsymbol{\zeta})|^2 S_T(\boldsymbol{\zeta} + \partial_{\mathbf{x}'} \Delta_{jk}(0, \boldsymbol{\zeta})) d\mathbf{x}' d\boldsymbol{\zeta}. \quad (\text{C.15})$$

Appendix D. The stationary phase calculation of I_3

Consider

$$I_3 = 2 \sum_{k=1, k \neq j}^4 \operatorname{Re} \int \mathbb{E}[(\mathcal{K}_j \mathcal{F}_j)[T](z) - T_{\Omega'_z}(z)] \mathcal{K}_j \mathcal{F}_k[T](z) dz. \tag{D.1}$$

We compute

$$\tilde{S}_{T, \tilde{T}_{jk}}(\zeta, \zeta') = \int \mathbb{E}[e^{i(x \cdot \zeta - x' \cdot \zeta')} T(x) e^{-i \Delta_{jk}(x', \xi')} T(x')] dx dx'. \tag{D.2}$$

Making use of expansion (C.5) and as before ignoring the first term and the higher order terms, we obtain

$$\approx \tilde{S}_T(\zeta, \zeta' + \partial_{x'} \Delta_{jk}(0, \xi')). \tag{D.3}$$

Now we have

$$\begin{aligned} I_3 \approx 2 \sum_{k=1, k \neq j}^4 \operatorname{Re} \int e^{i[(x-z) \cdot \xi - (x'-z) \cdot \xi' - x \cdot \zeta + x' \cdot \zeta']} \overline{B_j(z, \xi') A_k(x', \xi')} \\ \times |J_j(x', z, \xi')| (B_j(z, \xi) A_j(x, \xi) |J_j(x, z, \xi)| - 1) \\ \times \tilde{S}_T(\zeta, \zeta' + \partial_{x'} \Delta_{jk}(0, \xi')) dx dx' d\xi d\xi' d\zeta d\zeta' dz. \end{aligned} \tag{D.4}$$

The phase function is the same as φ_3 in equation (C.9) and so the critical points are as in (C.10).

Applying the method of the stationary phase, we obtain

$$\begin{aligned} I_3 \approx 2 \sum_{k=1, k \neq j}^4 \operatorname{Re} \int e^{ix' \cdot (\zeta' - \zeta)} (B_j(x', \zeta) A_k(x', \zeta) |J_{pq}(x', z, \xi')| - 1) \\ \times \overline{B_j(x', \zeta) A_j(x', \zeta)} |J_j(x', x', \zeta)| \tilde{S}_T(\zeta, \zeta' + \partial_{x'} \Delta_{jk}(0, \zeta)) dx' d\zeta d\zeta'. \end{aligned} \tag{D.5}$$

The leading-order contribution to this integral is when $\zeta = \zeta'$ because of the oscillatory term $e^{ix' \cdot (\zeta' - \zeta)}$ in the integral. Hence, we have the term $\tilde{S}_T(\zeta, \zeta + \partial_{x'} \Delta_{jk}(0, \zeta))$ in the integrand and assuming stationarity of \tilde{S}_T , this is 0. Therefore there is no leading order contribution of this integral to the determination of the filter B_j .

Appendix E. Variational derivative

We have $I(B_j) \approx I_1 + I_2 + I_4$. Let us write

$$\begin{aligned} I(B_j) = \int |B_{pq}(x', \zeta) A_j(x', \zeta) |J_j(x', x', \zeta)| - 1|^2 S_T(\zeta) dx' d\zeta \\ + \sum_{k=1, k \neq j}^4 \int |A_k(x', \zeta) B_j(x', \zeta) J_j(x', x', \zeta)|^2 S_T(\zeta + \partial_{x'} \Delta_{jk}(0, \zeta)) dx' d\zeta \\ + \int |B_j(x', \zeta)|^2 S_n(\zeta) |J_j(x', x', \zeta)| dx' d\zeta. \end{aligned} \tag{E.1}$$

Fix a function $B_0(x', \zeta)$ and for small ε consider a variation of the form $B_\varepsilon = B_j + \varepsilon B_0$. We substitute this into the above equation and differentiate with respect to ε and then set $\varepsilon = 0$.

We have

$$\begin{aligned}
 I(B_j + \varepsilon B_0) &= \int |(B_j + \varepsilon B_0)(\mathbf{x}', \zeta) A_j(\mathbf{x}', \zeta) |J_j(\mathbf{x}', \mathbf{x}', \zeta)| - 1|^2 S_T(\zeta) d\mathbf{x}' d\zeta \\
 &+ \sum_{k=1, k \neq j}^4 \int |A_k(\mathbf{x}', \zeta) (B_j + \varepsilon B_0)(\mathbf{x}', \zeta) J_j(\mathbf{x}', \mathbf{x}', \zeta)|^2 \\
 &\times S_T(\zeta + \partial_{\mathbf{x}'} \Delta_{jk}(0, \zeta)) d\mathbf{x}' d\zeta \\
 &+ \int |(B_j + \varepsilon B_0)(\mathbf{x}', \zeta)|^2 S_n(\zeta) |J_j(\mathbf{x}', \mathbf{x}', \zeta)| d\mathbf{x}' d\zeta. \tag{E.2}
 \end{aligned}$$

We differentiate $I(B_j + \varepsilon B_0)$ with respect to ε and set $\varepsilon = 0$. We obtain

$$\begin{aligned}
 0 &= 2 \operatorname{Re} \int (B_j(\mathbf{x}', \zeta) A_j(\mathbf{x}', \zeta) |J_j(\mathbf{x}', \mathbf{x}', \zeta)| - 1) \\
 &\times \overline{B_0(\mathbf{x}', \zeta) A_j(\mathbf{x}', \zeta) |J_j(\mathbf{x}', \mathbf{x}', \zeta)|} S_T(\zeta) d\mathbf{x}' d\zeta \tag{E.3}
 \end{aligned}$$

$$\begin{aligned}
 &+ \sum_{k=1, k \neq j}^4 2 \operatorname{Re} \int B_j(\mathbf{x}', \zeta) \overline{B_0(\mathbf{x}', \zeta)} |A_k(\mathbf{x}', \zeta) J_j(\mathbf{x}', \mathbf{x}', \zeta)|^2 \\
 &\times \tilde{S}_T(\zeta + \partial_{\mathbf{x}'} \Delta_{jk}(0, \zeta), \zeta' + \partial_{\mathbf{x}'} \Delta_{jk}(0, \zeta)) d\mathbf{x}' d\zeta d\zeta' \tag{E.4}
 \end{aligned}$$

$$+ 2 \operatorname{Re} \int B_j(\mathbf{x}', \zeta) \overline{B_0(\mathbf{x}', \zeta)} S_n(\zeta) |J_j(\mathbf{x}', \mathbf{x}', \zeta)| d\mathbf{x}' d\zeta. \tag{E.5}$$

Since this is 0 for all B_0 , we have,

$$\begin{aligned}
 0 &= (B_j(\mathbf{x}', \zeta) A_j(\mathbf{x}', \zeta) |J_j(\mathbf{x}', \mathbf{x}', \zeta)| - 1) \times \overline{A_j(\mathbf{x}', \zeta) |J_j(\mathbf{x}', \mathbf{x}', \zeta)|} S_T(\zeta) \\
 &+ \sum_{k=1, k \neq j}^4 B_j(\mathbf{x}', \zeta) |A_k(\mathbf{x}', \zeta) J_j(\mathbf{x}', \mathbf{x}', \zeta)|^2 S_T(\zeta + \partial_{\mathbf{x}'} \Delta_{jk}(0, \zeta)) \\
 &+ B_j(\mathbf{x}', \zeta) S_n(\zeta) |J_j(\mathbf{x}', \mathbf{x}', \zeta)|. \tag{E.6}
 \end{aligned}$$

Canceling out the Jacobian term and rearranging, we obtain

$$B_j(\mathbf{x}', \zeta) = \frac{\overline{A_j(\mathbf{x}', \zeta)} S_T(\zeta)}{\Psi} \tag{E.7}$$

where

$$\Psi = |J_j(\mathbf{x}', \mathbf{x}', \zeta)| \left[|A_j(\mathbf{x}', \zeta)|^2 S_T(\zeta) + \sum_{k=1, k \neq j}^4 |A_k(\mathbf{x}', \zeta)|^2 S_T(\zeta + \partial_{\mathbf{x}'} \Delta_{jk}(0, \zeta)) \right] + S_n(\zeta). \tag{E.8}$$

Taking into account the data collection manifold (30) and putting a characteristic function cut-off for those ζ that belong to this set, we arrive at (65).

References

- [1] Capozzoli A, Curcio C, D'Elia G, Di Vico A, Liseno A and Vinetti P 2009 NUFFT-based imaging of vegetation on graphic cards *Proc. 7th Int. Conf. Antenna Theory and Technology, (Lviv, Ukraine, 6–9 Oct. 2009)* pp 265–7
- [2] Cheney M and Bonneau R J 2004 Imaging that exploits multipath scattering from point scatterers *Inverse Problems* **20** 1691–711

- [3] Cheney M and Yazici B 2006 Radar imaging with independently moving transmitters and receivers *Proc. Defense Application of Signal Processing (DASP) Workshop (Melbourne, 10–14 December 2006)*
- [4] Duistermaat J J 1996 *Fourier Integral Operators (Progress in Mathematics vol 130)* (Boston, MA: Birkhäuser)
- [5] Gaburro R and Nolan C J 2008 Enhanced imaging from multiply scattered waves *Inverse Probl. Imaging* **2** 225–50
- [6] Garren D A 2002 SAR image formation uncorrupted by multiple-bounce artifacts *Radar Conf., Proc. IEEE* pp 338–43
- [7] Garren D A and Goldstein J S 2002 Extraction of multiple-bounce artifacts in tomographic imaging *Image Processing. Proc. Int. Conf.* vol 2 pp 613–6
- [8] Garren D A and Goldstein J S 2002 Image reconstruction without multiple-bounce ghosting artifacts *Biomedical Imaging. Proc. IEEE Int. Symp.* pp 1001–4
- [9] Garren D A, Goldstein J S, Obuchon D R, Greene R R and North J A 2004 SAR image formation algorithm with multipath reflectivity estimation *Radar Conf. Proc. IEEE (26–29 April 2004)* pp 323–8
- [10] Garren D A, Sullivan D P, North J A and Goldstein J S 2005 Image preconditioning for a SAR image reconstruction algorithm for multipath scattering *Radar Conf. IEEE Int. (9–12 May 2005)* pp 300–5
- [11] Grigis A and Sjöstrand J 1994 *Microlocal Analysis for Differential Operators (London Mathematical Society Lecture Note Series vol 196)* (Cambridge: Cambridge University Press)
- [12] Gustafsson M 2004 Multi-static synthetic aperture radar and inverse scattering *Technical Report LUTEDX/(TEAT-7123)* pp 1–28
- [13] Krishnan V, Swoboda J, Yarman C E and Yazici B 2010 Multi-static synthetic aperture radar image formation *IEEE Trans. Image Process.* **19** 1290–306
- [14] Linnehan R and Schindler J 2010 Validating multipath responses of moving targets through urban environments *IEEE Radar Conf. (10–14 May 2010)* pp 1036–41
- [15] Moses R L and Potter L C 2005 Noncoherent 2D and 3D SAR reconstruction from wide angle measurements *13th Annual Adaptive Sensor Array Processing Workshop (ASAP 2005)*
- [16] Nilsson S 1997 Application of fast backprojection techniques for some inverse problems of integral geometry *PhD Thesis* Linköping Studies in Science Technology, Linköping University (Dissertation No 499)
- [17] Nolan C J, Cheney M, Dowling T and Gaburro R 2006 Enhanced angular resolution from multiply scattered waves *Inverse Problems* **22** 1817–34
- [18] Obuchon D R, Garren D A, Goldstein J S, Greene R R and North J A 2004 Drift inversion estimation of multipath ghosts in SAR image reconstruction *Radar Conf., Proc. IEEE, (26–29 April 2004)* pp 556–8
- [19] Setlur P, Amin M and Ahmad F 2010 Multipath doppler signatures from targets moving behind walls *Radar Conf. IEEE (10–14 May 2010)* pp 799–803
- [20] Trèves F 1980 *Introduction to Pseudodifferential and Fourier Integral Operators* vol 1 (New York: Plenum)
- [21] Trèves F 1980 *Introduction to Pseudodifferential and Fourier Integral Operators* vol 2 (New York: Plenum)
- [22] Yarman C E, Yazici B and Cheney M 2008 Bistatic synthetic aperture radar imaging for arbitrary flight trajectories *IEEE Trans. Image Process.* **17** 84–93
- [23] Yazici B, Cheney M and Yarman C E 2006 Synthetic-aperture inversion in the presence of noise and clutter *Inverse Problems* **22** 1705–29